CHALMERS
UNIVERSITY OF TECHNOLOGY

Electrical Modelling of High-speed Photodiodes

Master's thesis in Master Wireless Photonics and Space Engineering

Geo Philip Muppathiyil

DEPARTMENT OF MICROTECHNOLOGY AND NANOSCIENCE
CHALMERS UNIVERSITY OF TECHNOLOGY
Gothenburg, Sweden 2024
www.chalmers.se

Master’s thesis 2024

Electrical Modelling of High-speed Photodiodes

Geo Philip Muppatiyil

Department of Microtechnology and Nano Science
Chalmers University of Technology
Gothenburg, Sweden 2024

Electrical Modelling of High-speed Photodiodes
Geo Philip Muppathiyil

Supervisor: Filip Hjort, Nvidia
Examiner: Magnus Karlsson, Department of Microtechnology and Nano Science

Master's Thesis 2024
Department of Microtechnology and Nano Science
Chalmers University of Technology
SE-412 96 Gothenburg
Telephone +46 31 772 1000

Cover:

Typeset in LaTeX
Printed by Chalmers Reproservice
Gothenburg, Sweden 2024

Electrical Modelling of High-speed Photodiodes
Geo Philip Muppathiyil
Department of Microtechnology and Nanoscience
Chalmers University of Technology

Abstract

Photodiodes are pivotal components in optoelectronic systems, converting light into electrical signals with applications spanning from telecommunications to medical devices. This thesis presents a comprehensive study on the electrical modeling of photodiodes, aiming to enhance their performance when integrated with transimpedance amplifiers (TIAs) in receivers.

The research commences with an in-depth analysis of the physical principles governing photodiode operation. Various modeling techniques are examined, with a particular emphasis on equivalent circuit models that accurately represent the photodiode's behavior under different biasing conditions.

The model is constructed based on experimentally measured frequency response and single-port reflection of the device. Devices with varying optical apertures and different biasing pads are analyzed. It is observed that the ground-signal pad geometry introduces additional inductance to the electrical model, enhancing the frequency response by up to 5 GHz compared to the ground-signal-ground pads. The study also compares the performance of several photodiode prototypes, varying parameters such as absorber thickness and extraction layer thickness. Furthermore, the combined response of the photodiode and TIA was simulated. The results indicate that the frequency response, when combined with the TIA for ground-signal pad geometry, remains flat up to 35 GHz, outperforming the ground-signal-ground design. This ensures that the receiver is free from frequency-dependent distortions. The responsivity and dark current characteristics of the devices are also measured.

In conclusion, the electrical modeling techniques presented in this thesis offer a powerful framework for understanding the photodiode performance with TIA in optical recievers. The findings contribute to the advancement of optoelectronic technology, paving the way for more efficient and versatile applications in various fields such as data centers and other high-speed communication systems.

Keywords: Photodiode, Frequency response, scattering parameters, Transimpedance amplifier, Absorber layer, Extraction layer, Ground-signal, Ground-signal-ground, Voltage-controlled current source

Acknowledgements

I would like to express my deepest gratitude to my supervisors, Filip Hjort and Anders Larsson, whose expertise, understanding, and patience added considerably to my graduate experience. Their guidance and support were invaluable in navigating the complexities of my research and in the completion of this thesis.

I am also profoundly grateful to my thesis examiner, Prof. Magnus Karlsson for his insightful comments, and encouragement.

Special thanks to Nvidia, where I conducted my research. I am particularly indebted to my manager, Isabelle Cestier and other colleagues, for their continuous support, valuable insights, and for providing me with the resources necessary to complete my research. The collaborative environment and professional guidance I received were crucial to the success of this project.

I would also like to acknowledge the support of my colleagues and friends, Attila, Ravindu, Ashuthosh, Ali, Dennis, and Hans who provided me with assistance, encouragement, and a sense of camaraderie throughout this journey. Their support made the challenging moments more manageable and the successes more enjoyable. I am deeply thankful to my family, especially my wife Kavya, and our kids Liana and Liam, for their unwavering support, love, and encouragement. Their belief in me has been a constant source of motivation and strength.

Finally, I would like to extend my appreciation to all those who have supported me in any respect during the completion of this project. Your encouragement and support have been greatly appreciated.

Geo Philip Muppathiyil, Gothenburg, Aug 2024

List of Acronyms

Below is the list of acronyms that have been used throughout this thesis listed in alphabetical order:

AI	Artificial Intelligence
MM	Multi mode
VCSEL	Vertical Cavity Surface Emitting Laser
PD	Photodiode
e-h	electron hole
TIA	Transimpedance amplifiers
S	Scattering parameter
eV	Electron volt
UTC	Uni-traveling-carrier
VOA	Variable Optical Attenuators
OSA	Optical Spetrum Analyser
SHG	Second Harmonic Generation
GSG	Ground-Signal-Ground
GS	Ground-signal
PM	Polarization maintaining
CW	Continuous wave
VNA	Vector Network Analyzer

Nomenclature

Below is the nomenclature of indices, sets, parameters, and variables that have been used throughout this thesis.

Indices

i,j	Indices for distribution network buses

Parameters

h	Planks constant
c	Velocity of light
k	Boltzman constant
α	Absorption coefficient
η	Quantum efficiency

Variables

I_{ph}	Photocurrent
i_d	Dark current
I_B	Background current
R	Responsivity
P_{in}	Input power
ω	Angular frquency
λ	Wavelength
B	Bandwidth
T	Absolute Temperature
ν	Frequency

A	Area
ϵ	Permittivity

Contents

List of Figures

List of Tables

1

Introduction

The increasing demand for high data rates and high-quality transmission, coupled with the proliferation of large-capacity data storage, sensing capabilities, and imaging technologies, presents novel challenges for existing communication systems. While standardized 100-GBaud transmission schemes are available [1], recent publications have already demonstrated successful transmission experiments using symbol rates of up to 200 GBaud for both coherent and direct detection schemes. Recent advancements in AI have been nothing short of revolutionary, particularly in the realms of generative AI and machine learning. These technologies are not only transforming the way we interact with data but are also driving an unprecedented demand for high-speed data centers. As artificial intelligence (AI) models grow in complexity and the datasets they process expand exponentially, the need for rapid data transfer within and between data centers has become critical [2]. Moreover, the AI boom is coinciding with a period of intense growth in the data center market, with expectations for the hyper scale data center market to grow at an impressive 20 percent compound annual growth rate[3]. As we continue to push the boundaries of what AI can achieve, the symbiotic relationship between AI innovation and the capabilities of data centers will remain a pivotal focus for the tech industry. The need for 100Gb/s per lane multimode (MM) vertical-cavity surface-emitting lasers (VCSELs) and associated receivers remains strong, particularly in data centers, cloud storage, and enterprise networks. VCSEL-based multimode links, known for their cost-effectiveness and energy efficiency, are especially well-suited for high-speed interconnections (HSI) that support generative AI [4]. These advancements have been facilitated by the accessibility of high-speed components [5, 6]. From the receiver's perspective, where the photodiode (PD) plays a central role, its performance significantly impacts data speed scaling and overall system efficiency.

Photodiodes serve as a crucial component in the receiver chain of a system. Their primary function is to convert optical signals, whether analog or digital, into electrical signals, typically manifested as a photocurrent. The fundamental physical process underlying semiconductor detectors involves the optical generation of electron-hole (e-h) pairs through the absorption of incident photons. Subsequently, the photogenerated e-h pairs are separated and directed toward the external circuit via an electric field. This collecting field can be generated by applying an external voltage bias across a reverse-biased junction, as observed in configurations such as PN (p-type and n-type) and PIN (p-type, intrinsic, and n-type).

Physics-based models including fundamental physical partial differential equations, such as diffusion and transport equations [7, 8], are often used to accurately predict the electrical behavior of semiconductor devices and can be used to minimize the costly and time-consuming test wafer runs involved in the development of new PDs. However, a photodiode's performance is influenced not only by the device itself but also by the external microwave circuits, often resulting in discrepancies between simulations and measurements. To improve numerical modeling accuracy, researchers employ equivalent circuit models that integrate microwave circuit simulations to analyze the photodiode's performance. This analytical approach simplifies the photoelectric conversion problem into a purely electrical one, enabling concise and effective simulation of high-frequency device characteristics. By analyzing parameters within the circuit model, accurate device behavior under various conditions can be obtained [9].

A precise equivalent circuit model better reflects the device's physical characteristics, guiding subsequent analysis and optimization processes. Understanding the full scattering (S) parameters of a photodiode is crucial for designing and modeling optical receivers, as the electrical interaction between the photodiode and trans-impedance amplifiers (TIA) significantly influences receiver performance [10]. While modeling using measured S-parameters alone is possible, having a reliable equivalent circuit that explains observed photodiode behavior is preferable. The utilization of a simple RC circuit plus transit time model [11] has proven insufficient to effectively fit the measured S11 impedance and provide a precise understanding of the factors limiting bandwidth in PIN detectors.

This research project represents a significant effort in developing a model for photodiodes by leveraging their electrical analogs. Specifically designed for use in optical receivers operating around the 1000 nm wavelength range, they are intended to be paired with vertical-cavity surface-emitting lasers as transmitters. The primary objective is to explore the performance characteristics of photodiodes when integrated with TIAs. The model development is based on measured S22 parameters of the photodiode device and frequency response measurements. A meticulous analysis of the microwave circuitry associated with the photodiode is conducted, with a specific focus on understanding how its geometry impacts effective bandwidth. Additionally, the study investigates photodiodes with varying absorber thickness and collector thickness to determine optimal performance in conjunction with TIAs.

2

Theory

This chapter provides a concise overview of photodiode (PD) operation, various characteristic parameters, and the methodology for constructing an electrical equivalent circuit.

2.1 Physics of Photodiodes

PDs serve as the initial component in the system receiver chain. Their primary function is to convert optical signals (whether analog or digital) into electrical signals, typically manifested as a photocurrent (I_{ph}). The fundamental mechanism underlying semiconductor detectors involves the optical generation of electron-hole (e-h) pairs through the absorption of incident photons (Figure 2.1). These photogenerated e-h pairs are subsequently separated and collected by an electric field, which can be induced either by an external voltage bias in a reverse-biased junction. In certain cases, an additional step follows photogeneration and collection: the photocurrent undergoes amplification through external or built-in gain processes.

In the absence of illumination, detectors exhibit an output current known as the dark current (i_d). Meanwhile, the photocurrent typically demonstrates a linear

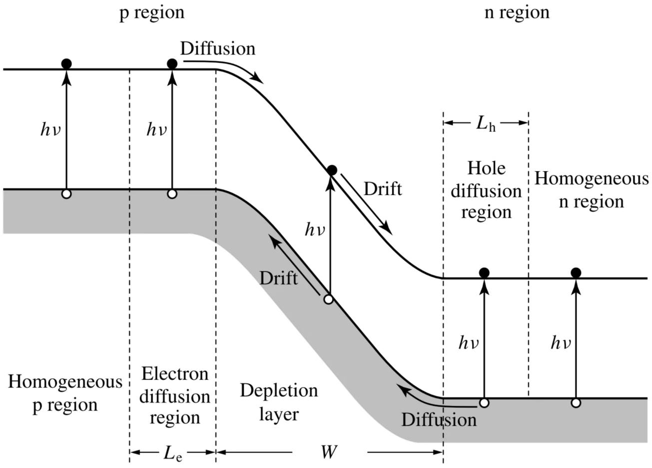

Figure 2.1: Photocarriers generation mechanism up on illumination for a standard PN junction device [12].

relationship with the input optical power,

$$I_{ph} = RP_{in}, \tag{2.1}$$

where R represents the responsivity of the device and P_{in} is the incident optical power. However, when exposed to high input optical power, the photogenerated carriers effectively shield the collecting electric field, resulting in current saturation. The photocurrent is contingent upon the quantity of photogenerated carriers, which, in turn, relies on the material's absorption profile relative to the wavelength (λ) of the modulated optical carrier. Consequently, the responsivity exhibits wavelength-dependent behavior, characterized by a bandpass response. In the context of quasi-static and memoryless behavior, the validity of relation (2.1) is maintained when the optical power changes gradually over time. For time-harmonic input optical power, this relation remains valid as long as the modulation frequency is lower than the device cutoff frequency. However, when the input power varies rapidly, the output current no longer tracks its instantaneous value. This discrepancy arises due to low-pass or delay mechanisms, including the effects of device capacitance and finite transit time for photocarriers before collection. In small-signal conditions and for harmonic input optical power, we can define a frequency domain (complex) responsivity ($R(\omega)$). This responsivity relates the amplitude and phase of the small-signal photocurrent component at angular frequency (ω) to the amplitude and phase of the harmonic input optical power. Notably, the function $R(\omega)$ typically exhibits low-pass behavior.

2.1.1 Material Selection

The relationship between the optical absorption coefficient and wavelength is illustrated in Figure 2.2 for various photodiode materials. The curves show that the absorption coefficient (α_s) exhibits strong wavelength dependence. Consequently, each semiconductor material is suitable only within a specific wavelength range. The upper wavelength limit (λ_c) is determined by the material's bandgap energy (E_g), as the photon energy must be greater than the bandgap energy to create an e-h pair for conduction. When expressing in electron volts (eV), λ_c can be calculated in micrometers (μm) using the following equation,

$$\lambda_c(\mu m) = \frac{hc}{E_g} = \frac{1.2406}{E_g(eV)}. \tag{2.2}$$

The cutoff wavelengths are approximately 1.06 μm for silicon (Si), 1.6 μm for germanium (Ge), and 1.7 μm for indium gallium arsenide (InGaAs). The absorption spectrum of InGaAs is contingent upon its compositional ratio. Specifically, the $In_{0.53}Ga_{0.47}As$ variant aligns with the lattice structure of InP, ensuring compatibility. Beyond these wavelengths, the photon energy is insufficient to promote an electron from the valence band to the conduction band. Conversely, at shorter wavelengths, the photoresponse diminishes due to photon absorption near the photodetector surface, where the recombination time for generated electron-hole pairs is very brief. Consequently, the carriers recombine before the photodetector circuitry can collect them.

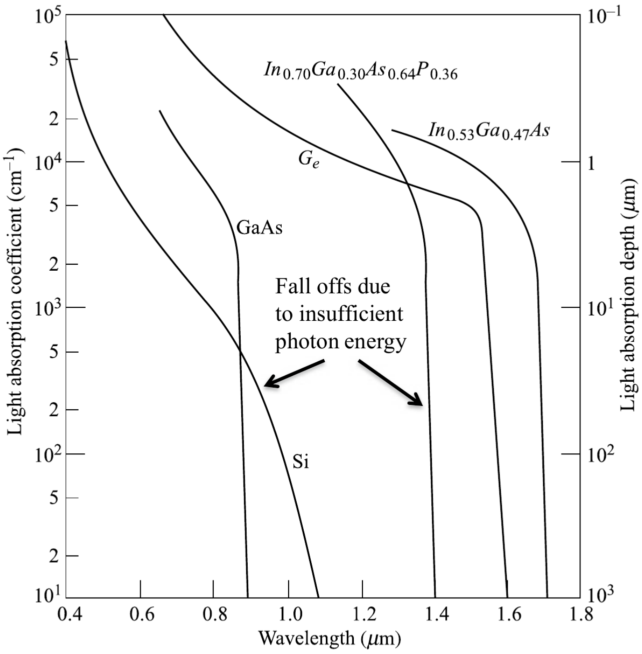

Figure 2.2: Optical absorption coefficient as a function of wavelength of different photodetector materials [13].

2.1.2 Bandgap Engineered PDs

Conventional junction photodiodes encounter challenges related to the width of the depletion region and the extended time required for charge carrier diffusion. In contrast, bandgap-engineered PDs, such as PIN and UTC(Uni-traveling-carrier) PDs, are specifically designed to address these issues and enhance both frequency response and responsivity.

The band diagrams for PIN–PD [14] and UTC–PD [15] are shown in Figure 2.3. The PIN–PD has a straightforward three-layer structure, consisting of wide-bandgap P- and N-layers along with a depleted absorber. In the depleted absorber of the PIN–PD, both holes and electrons contribute to the photoresponse. However, the output response primarily depends on the low-velocity carrier holes. Their transport velocity is an order of magnitude lower than that of electrons, which limits the overall photoresponse. The band structure of UTC–PD, achieved by dividing the PIN–PD absorber into two layers, consists of a p-type neutral absorber and a wide-bandgap (depleted) carrier collector [17]. By employing bandgap grading or doping in the absorber, a quasi-field is formed to effectively reduce the electron traveling time. Meanwhile, the photogenerated holes in the InGaAs absorber respond rapidly within several picoseconds due to the high concentration of holes. This negligible effect on the photoresponse allows the high-velocity electrons to dominate the overall response in UTC–PDs. Additionally, quasi-ballistic transport (overshoot velocity) occurs in the InP collector, resulting in a very short total delay time for the entire UTC–PD. When comparing PIN–PD and UTC–PD with the same absorber width (W_a), the UTC–PD (with ($W_a = W_c$)) exhibits superior frequency response due to the shorter

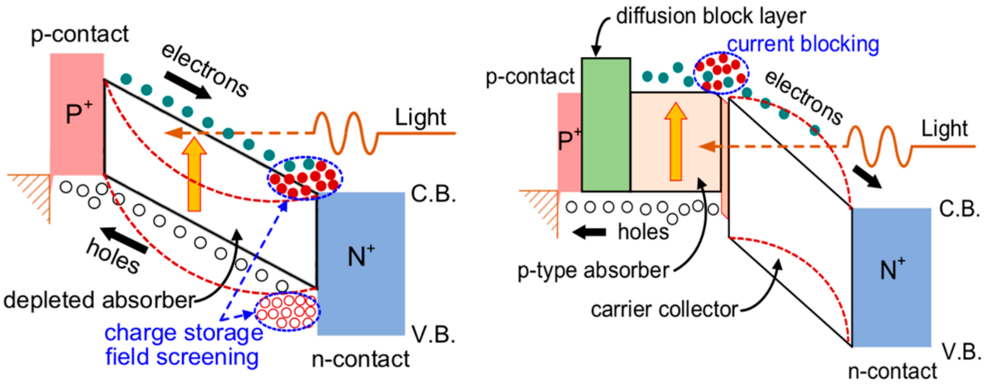

(a) **(b)**

Figure 2.3: Band diagrams of (a) PIN-PD,(b) UTC-PD [16].

traveling time in the collector. This advantage arises from the significant difference in carrier velocities, even though carriers in UTC–PD travel approximately three times the average distance compared to those in PIN–PD.
The photodiode aperture must be sufficiently large to accommodate misalignments in the supporting optics or to efficiently collect light from an optical fiber operating in multimode conditions. Additionally, there are novel modified PIN diodes with separate light absorption and electron drift/collector regions [18]. Similar to UTC PDs these devices take advantage of the high absorption properties of InGas at lower wavelengths (980-1060 nm) and the peak electron drift velocity in InP under specific electric field conditions. Figure 2.4 shows the schematic of the energy level diagram of this modified PIN PD with separate light absorption and drift regions, where the arrow marks the position of a thin n-type layer that controls how the voltage drop is divided between the absorber and collector.

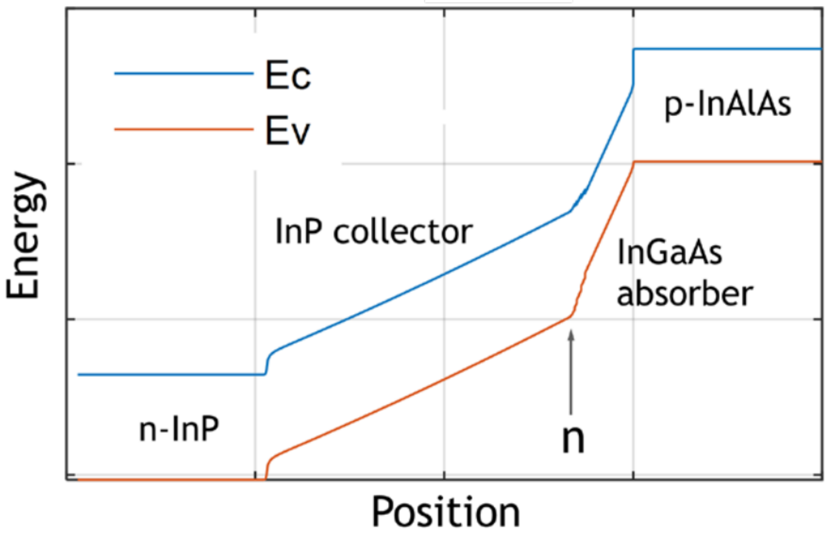

Figure 2.4: Energy level diagram of separate absorption and drift region PD.

2.1.3 Channel capacity of a Photodiode

The maximum data rate of a communication channel, often referred to as the channel capacity C of a communication system is given by the Shannon-Hartley relation [19],

$$C = B\ \log_2(1 + \frac{S}{N},) \tag{2.3}$$

where B represents the bandwidth, S and N represent signal and noise power respectively. Substituting the expressions for S and N for a PIN photodiode,

$$C = B\ \log_2(1 + \frac{R^2 P_{in}^2}{2q(RP_{in} + i_D)B + 4k_B TB/R_L}), \tag{2.4}$$

where i_D is the dark current of the PD. k_B represents the Boltzmann constant, T is the absolute temperature and R_L stands for the load resistance. Equation 2.4 [19] demonstrates that while dark current and background noise do impact channel capacity, frequency bandwidth, and responsivity play a more crucial role in achieving maximum channel capacity.

2.2 Photodiode Characteristic Parameters

2.2.1 Quantum efficiency and responsivity

The quantum efficiency η of a photodiode relates to the photodiode's ability to convert optical energy into electrical energy, which is defined as:

$$\eta = \frac{\text{number of e-h pairs created}}{\text{number of photons incident}}, \tag{2.5}$$

$$\eta = \frac{\frac{I_{ph}}{q}}{\frac{P_{in}}{h\nu}}, \tag{2.6}$$

where I_{ph} is the photo-induced current, P_{in} is the incident optical power, q is the elementary charge, h is the Planck's constant, and ν is the frequency of the incident radiation. Instead of the quantum efficiency η, the responsivity R (Equation 2.1) is often used,

$$R = \frac{q\eta}{h\nu}. \tag{2.7}$$

For an ideal photodiode, the output photocurrent (I_{ph}) exhibits linearity with the incident optical power (P_{in}). A photodiode is considered linear when its responsivity (R) is independent of input power. However, in practical scenarios, photodiodes exhibit linearity only within a specific range of incident optical power. The minimum incident optical power corresponds to the threshold of detectability, while the maximum incident optical power is limited by the photodiode's saturation point.

2.2.2 Frequency Response

The bandwidth of photodetectors is a critical performance metric across various applications. Researchers have extensively studied the limiting factors affecting response time and explored methods for improvement. Typically, a photodetector's response time relies on carrier transport within the device and the circuit dynamics described by the lumped element model. The 3-dB bandwidth serves as a useful characterization parameter, reflecting the upper limit of the photodetector's speed[20].

$$f_{\text{3-dB}} = \frac{1}{\sqrt{f_t^{-2} + f_{RC}^{-2}}}, \tag{2.8}$$

assuming Gaussian impulse response and transfer functions, the formula considers f_t as the transit time-limited bandwidth and f_{RC} as the RC time-limited bandwidth. The transit time refers to the duration it takes for photogenerated carriers (electrons and holes) to be collected within a photodiode. In an ideal PIN photodiode, this transit time is directly proportional to the thickness of the depletion region relative to the carrier velocity. Reducing the depletion region thickness increases the transit time-limited bandwidth, but it comes at the cost of lower quantum efficiency for a PIN PD whereas the quantum efficiency of the UTC-PD and separate absorption and drift region PD are predominantly controlled by the thickness of the absorber layer. Additionally, decreasing the depletion region thickness may lead to a larger junction capacitance, which in turn reduces the RC time-limited bandwidth. The RC time-limited bandwidth is often derived from the equivalent circuit model of the photodetector. The presence of junction capacitance, along with parasitic capacitance, creates a low-pass filter effect. Consequently, a smaller active area is preferred to achieve a high response speed as the junction capacitance of a PD scales linearly with the area.

The bandwidth of a short-pulse detector can be determined by applying an ultrashort optical pulse to the input and measuring the resulting current pulse duration at the output. The output pulse is passed through a load resistor (typically 50Ω) to generate a voltage pulse, which can be displayed and measured using an oscilloscope and transformed to the frequency domain by a Fourier transform. The detector's bandwidth is then defined as the frequency at which its response drops to 50% of its DC value. On a logarithmic scale, this corresponds to the -3 dB point of the voltage spectrum and is commonly referred to as the voltage bandwidth. In optical applications, this same measure of bandwidth is known as the optical bandwidth. In analog and microwave contexts, bandwidth is defined as the frequency where the output power decreases by 50% relative to its DC value. Again, on a logarithmic scale, this corresponds to the -3 dB point of the power spectrum and is referred to as the power bandwidth. Historically, this has also been termed the electrical bandwidth. Mathematically,

$$\text{-3 dB optical bandwidth} = \text{-6 dB electric bandwidth}, \tag{2.9}$$

due to the fact that electrical power is proportional to the square of optical power in the photodetection process.

2.3 Equivalent circuit model

The PIN–PD can be treated as a special case, consisting of a single intrinsic/depletion layer (W_a). The RC time-limited bandwidth (f_{RC}) and transit time-limited bandwidth (f_t) typically constitute the main 3-dB bandwidth of a PD. In this context, we neglect diffusion effects at high frequencies. Assuming that the PD has a single intrinsic layer (as shown in Figure 2.3) with thickness (d) and area (A), the RC time-limited bandwidth can be expressed as:

$$f_{RC} = \frac{1}{2\pi\ RC}, \tag{2.10}$$

where C is the PD capacitance (in the ideal case)and R is the sum of series resistance and the load resistance which is 50Ω and the diode junction capacitance is given by the relation,

$$C = \frac{\epsilon\ A}{d}, \tag{2.11}$$

with ϵ being the permittivity of the i-layer. It is important to note that (2.11) undergoes modification when a PD consists of multiple dielectric or depletion layers. In such cases, the corresponding values are replaced by the effective relative permittivity (ϵ_{re}) and the total depletion thickness (d_T), respectively. These adjustments are necessary for accurate modeling[22].

$$\epsilon_{re} = \frac{1}{\sum_{m=1}^{n} \frac{d_m}{\epsilon_r}}, \tag{2.12}$$

$$d_T = d_1 + d_2 + ... + d_n, \tag{2.13}$$

$$C = \frac{\epsilon_0 \epsilon_{re}\ A}{d_T}, \tag{2.14}$$

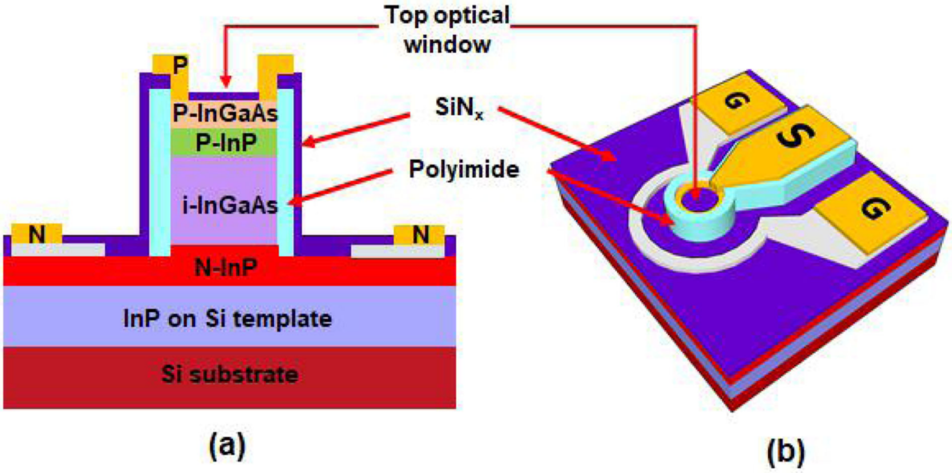

Figure 2.5: (a) Cross-section schematic of a mesa PD structure. (b) 3D schematic of a high-speed InGaAs PD on silicon [21].

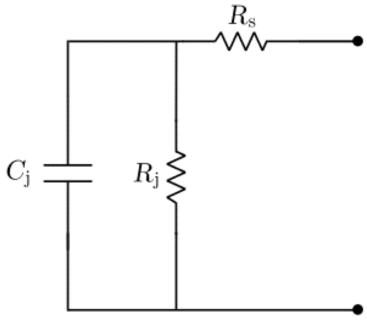

Figure 2.6: Simplest equivalent circuit for S22 of a PD.

and the 3dB bandwidth becomes

$$f_{3dB,RC} = \frac{d_T}{2\pi R \epsilon_0 \epsilon_{re} A}. \tag{2.15}$$

In this simple scenario, the input impedance of a PD should be represented by a very simple circuit as shown in Figure 2.6. However one needs to consider the associated microwave circuitry also to develop a practical equivalent circuit for a PD.

2.3.1 Time Delay equivalent circuits for PD

The time-delay equivalent circuit model for PIN–PDs has been thoroughly analyzed by Wang et al.[23, 24], and is depicted in Figure 2.7. Fundamentally, a basic PIN PD acts as a current generator. The corresponding equivalent circuit comprises three main components, as shown in Figure 2.7.

- The PD itself
- The coplanar waveguide (CPW)
- The load

The photocurrent is obtained and simulated using a current source (I_{ph}) in parallel with the junction capacitance (C_j) and a large shunt resistance, R_j (usually 100 kΩ). Additionally, a small series of resistances (R_{s1}, R_{s2}) accounts for the resistance of the PD including the depletion region and the ohmic contact resistance or metallic

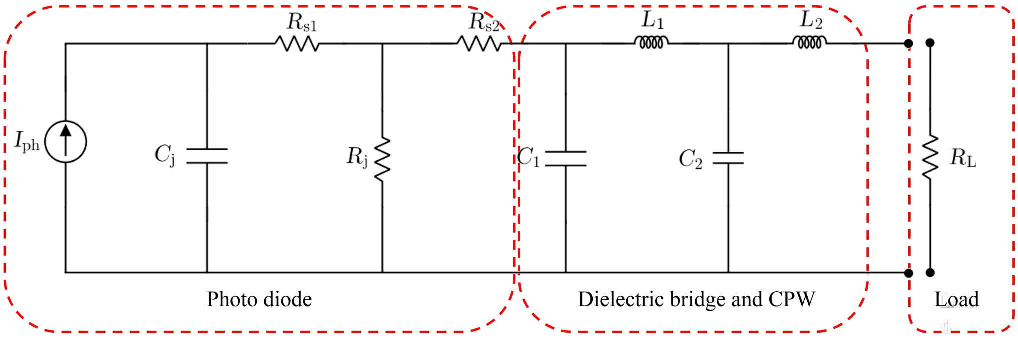

Figure 2.7: PD equivalent circuit with CPW and load.

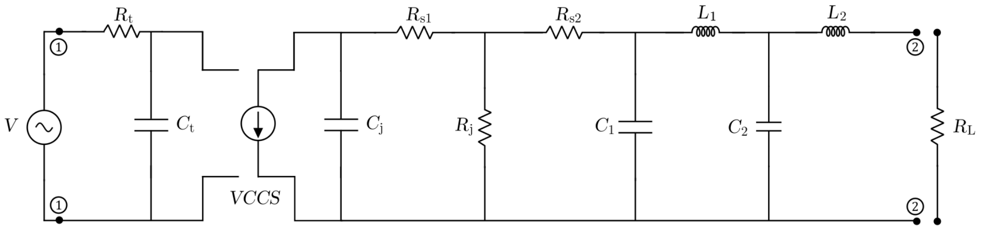

Figure 2.8: PD equivalent circuit considering the transit time, CPW, and load.

connections. The impedance of the CPW section depends strongly on the geometry and can affect the frequency response of the PD.

To evaluate the opto-microwave conversion properties of high-speed PDs, we can synthetically analyze S-parameters, including reflection coefficients (S_{22}), and optoelectronic conversion properties (S_{21}). The small-signal radio frequency (RF) equivalent circuit for the PD, considering both the carrier transit effect [25] and the external parasitic components [24] is given in Figure 2.8. The small-signal RF equivalent circuit given in Figure 2.8 uses a voltage-controlled current source (VCCS, $I_{ac} = g_m V_{ac}$, where g_m is the transconductance (taken to be 1 in this study), and V_{ac} is the voltage drop across C_t to replace the current source I_{ph}. R_t and C_t control the transit response of the device. The overall frequency response of the photodiode is influenced by several key factors, including the transit time bandwidth, RC bandwidth, coplanar waveguide, and load impedance properties. An advantage of using a simple time delay model lies in the ability to deduce lumped components from basic impedance and frequency response measurements. This derived model can then be effectively employed alongside available load properties (such as the small-signal model of the load) to characterize the collective behavior of the receiver system.

3

Methods

This chapter provides an account of the experimental procedure employed to measure the critical parameters of photodiodes for constructing their electrical equivalent circuit. As discussed in the preceding chapter, the electrical model is developed based on impedance and frequency response measurements. Additionally, the assessment encompasses the measurement of dark current (i_d) and responsivity (R), both of which play pivotal roles in characterizing photodiodes.

3.1 Frequency Response measurement

Accurate measurement of photoreceiver responses is essential for applications in high-speed optoelectronic systems. Historically, both impulse and heterodyne methods have been widely used to characterize high-speed photoreceivers. Heterodyne methods offer exceptional accuracy [26] but can be time-consuming, providing only the magnitude of the response. In contrast, time-domain measurements yield both magnitude and phase information rapidly [27]. Advanced time-domain techniques incorporate corrections for oscilloscope frequency response, jitter, and laser pulse width. Additionally, time-base distortion, electrical mismatch, and measurement nonlinearity[28] can also be addressed in time-domain measurements.
Considering a linear system with impulse response h and input x the output of the system is given by a convolution,

$$y(t) = \int x(\tau)h(t-\tau)\ d\tau. \tag{3.1}$$

In the Fourier domain,

$$Y(\omega) = X(\omega)H(\omega), \tag{3.2}$$

where $H(\omega)$ is frequency response of the system. The frequency response can be obtained by performing a discrete-time Fourier transform on the measured impulse response function. In this project, impulse measurements using a pulsed laser allow us to calculate the frequency response of the system.

3.1.1 Experimental procedure

At the core of the impulse measurement setup is a femtosecond laser system—the FemtoFiber Pro by TOPTICA Photonics. This laser employs a core-pumped fiber doped with Erbium ions as the active laser medium and non-linear processes subsequently produce laser output with a tunability in wavelength (850nm-1100nm)

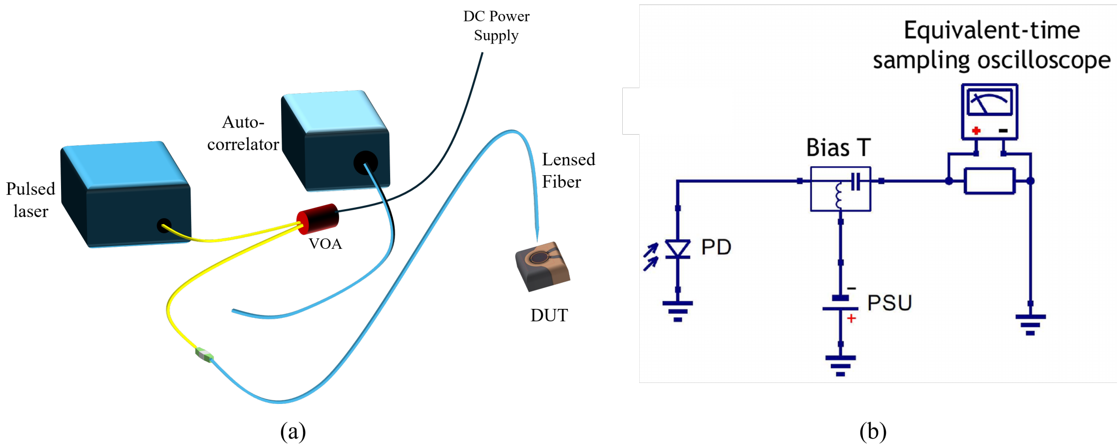

Figure 3.1: Schematic of the experimental arrangement (a) lensed fiber focusing the laser onto the device under test, (b)biasing and data collection.

and a pulse width of ∼ 1 ps. The laser output is extracted using a polarization-maintaining (PM) fiber and subsequently directed to the input side of the variable optical attenuator (VOA) model V800PA by Thorlabs. The VOA allows precise control of the output power through an external DC voltage. Figure 3.1 shows the schematic of the experimental arrangement to measure the frequency response of the PD. The output from the VOA is subsequently coupled to a (Yokogawa) optical spectrum analyzer (OSA). The next step is the pulse width measurement using an autocorrelator (APE pulseCheck 150). The operation of an autocorrelator for measuring pulse duration involves superimposing a pulse with a time-delayed replica of itself. These two pulses are then focused into a nonlinear crystal, such as a second harmonic generation (SHG) crystal, where they recombine both spatially and temporally, producing a third beam at twice the frequency of the original pulse. By varying the time delay, the temporal overlap of the two pulses changes, resulting in different interaction intensities. A detector measures the autocorrelation signal, which represents the overlap intensity as a function of the distance (delay) variation.

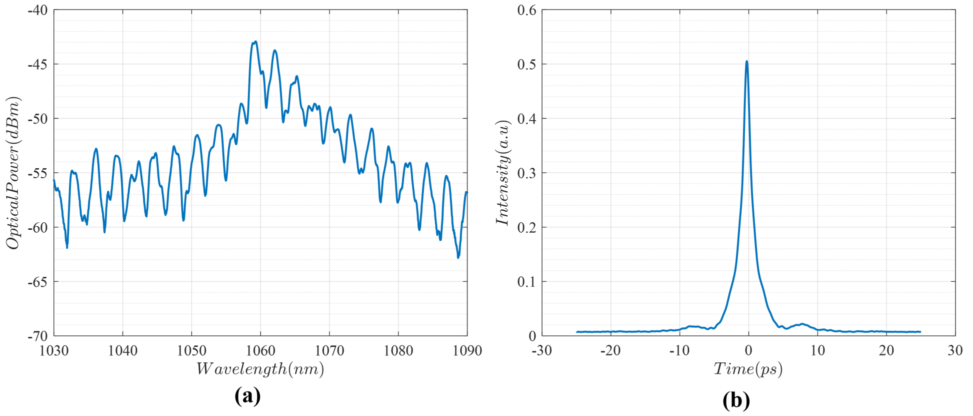

Figure 3.2: (a) Optical spectrum and (b) pulse width from the autocorrelator

Since the autocorrelation signal is proportional to the pulse duration, analyzing this signal enables the calculation of the pulse duration. The intensity autocorrelation (a special case of cross-correlation) of the laser pulse (signal shape) is given by,

$$A(t) = \int I(\tau)I(t-\tau)\ d\tau, \tag{3.3}$$

which in the Fourier domain becomes,

$$G(\omega) = F_I(\omega)F_I^*(\omega) =\mid F_I(\omega) \mid^2 . \tag{3.4}$$

The impact of the laser pulse shape can be de-embedded from the measured frequency response, $F(\omega)$, using the autocorrelator measurement, thus giving us the actual PD frequency response,

$$\mid H(\omega) \mid = \frac{\mid F(\omega) \mid}{\sqrt{\mid G(\omega) \mid}}. \tag{3.5}$$

Figure 3.2 shows the optical spectrum measured in the OSA and the autocorrelator pulse width measurement results.

Following spectrum and pulse width checks, the laser beam is directed into a lensed polarization-maintaining fiber. The lensed fiber focuses the fundamental fiber mode to a small area, significantly enhancing light coupling efficiency to the PD. The lensed fiber is securely mounted vertically on a three-axis stage with fine adjustments, ensuring precise alignment over the photodetector under test. Additionally, the PD is placed on a temperature-stabilized platform to maintain a constant temperature of 25^{o}C throughout the measurement. The biasing and output signal collection from

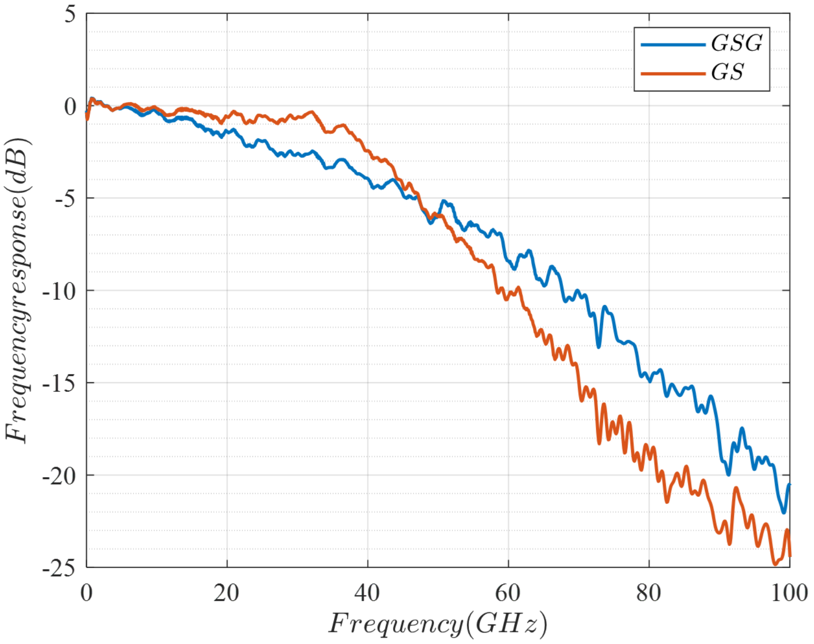

Figure 3.3: Frequency response of PD-A with GSG and GS probe measured at -2V biasing.

the photodetector is facilitated using either a GSG or GS probe, depending on the PD design. The probe is connected via a V-cable to a bias T, which effectively separates the DC biasing voltage from the high-frequency PD output. The resulting output signal from the bias T is then directed to an equivalent-time sampling scope for further analysis. After probing the photodetector (PD) using a microscope, we record its impulse response under various bias conditions. To analyze the frequency response, we perform a Discrete Fourier Transform (DFT) on the collected impulse response. Figure 3.3 shows the frequency response plots obtained for PD-A with GSG and GS probes with -2v biasing. The effect of the V-cable, bias T, and excitation pulse shape are de-embedded from the frequency response. The length of the PM fiber to the sample and the autocorrelator is kept the same to account for the dispersion-related pulse broadening in the fiber.

3.2 Responsivity Measurements

The responsivity of a photodiode represents the ratio of generated photocurrent to incident optical power. This measurement is typically performed within the linear response region. To determine the responsivity of the photodiode under test, we employ a continuous-wave (CW) 1064 nm laser. The input power of this laser is adjusted using a VOA, whose voltages are calibrated to specific power levels using a broad-area photodiode. After calibrating the VOA to specific power levels, we direct the laser beam into the vertically mounted PM lensed fiber with a spot size approximately 4 times smaller than the PDs' optical aperture. The position of the lensed fiber is adjusted while monitoring the reverse current to ensure maximum light coupling. Figure 3.4 shows an example measurement of the responsivity of PD-A with $20\mu m$ optical aperture.

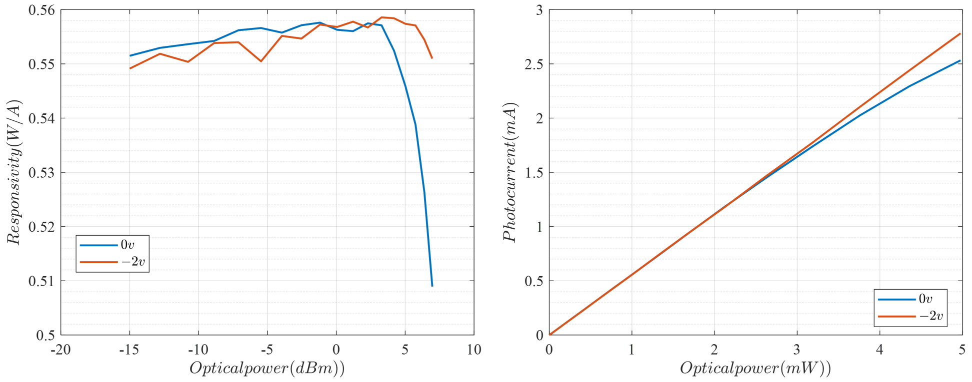

(a)

(b)

Figure 3.4: (a) Responsivity measurement of PD-A GS probe($20\mu m$),(b)plot between photocurrent vs optical power

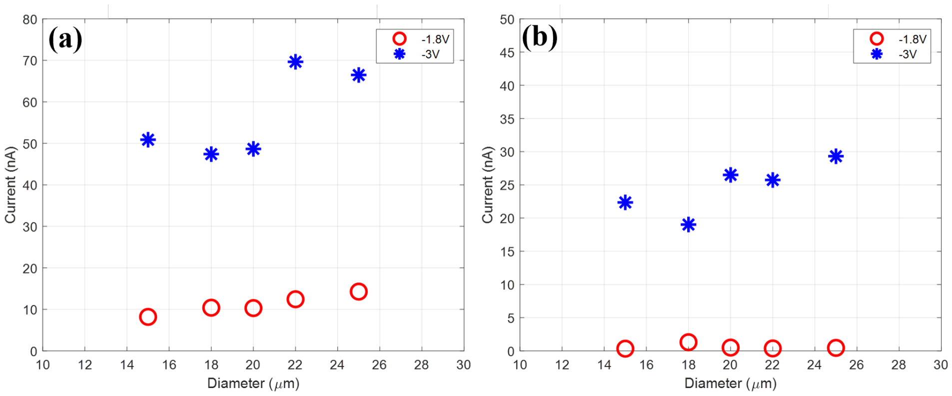

Figure 3.5: (a) Dark current for different optical aperture PD-A GS probe (20μm),(b) dark current of different optical aperture PD-B GS probe (20μm).

3.3 Dark Current Measurement

To measure dark current, the device under test is enclosed within a black box in a dark room, and the current passing through it is recorded at various biasing voltages using a source measurement unit with a sensitivity in the order of 10s of picoampere. Figure 3.5 illustrates the dark current for PD-A and PD-B under biasing conditions of -1.8V and -3V. The dark current for the PD-B design is an order of magnitude lower compared to PD-A. This reduction is likely attributed to the thicker absorber in PD-B, which results in a lower electric field for a given reverse bias voltage compared to the thinner absorber in PD-A.

3.4 Electrical reflection measurements (S22)

Single-port electrical reflection measurements, specifically S22 measurements, play a crucial role in constructing the electrical equivalent circuit of the photodiode. These measurements are conducted using a vector network analyzer (VNA). Prior to each measurement, the VNA is calibrated using a standard calibration substrate provided by the vendor. This calibration process effectively eliminates the impact of connection cables and probes, ensuring accurate and sensitive reflection measurements. Figure 3.6 shows example S22 measurements of PD-A (20μm, -2V bias) with GSG (ground-signal-ground) and GS (ground-signal) probes. The VNA measurements yield a complex reflection coefficient (S22) with a 50Ω load. S22 can be correlated to the device impedance and the load by the relation

$$S22 = \frac{Z_L - Z}{Z_L + Z}, \tag{3.6}$$

knowing S22 and the load the impedance of the device can be calculated as

$$Z = Z_L \frac{1 - S22}{1 + S22}, \tag{3.7}$$

The measured S22 of the device can be used to determine the parasitic components of the electric model. The optimization function in ADS is used to figure out the

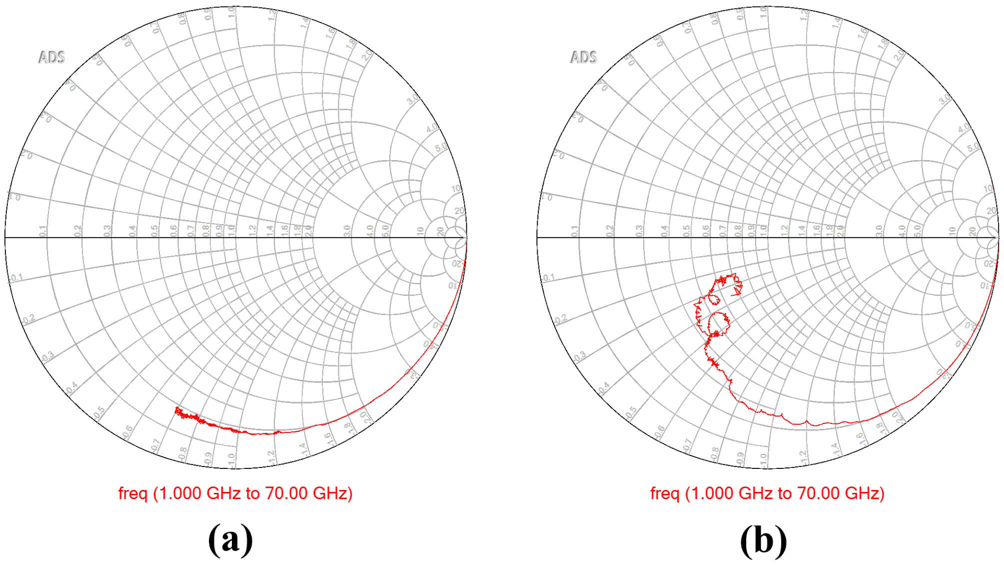

Figure 3.6: (a) S22 of GSG and (b) S22 of GS of 20μm PD-A biased at -2V.

component values of the circuit given in Figure 2.7. Once the parasitic components are fixed the transit part is extracted by de-embedding the parasitic response from the measured frequency response of the device. The high frequency reflection with GSG and GS probe shows a significant difference (GS shows higher noise at high frequency). This can be attributed to the better electric field confinement in the case of GSG and the higher inductive nature of GS which is predominant at high frequencies.

4

Results

This chapter delves into a systematic analysis of the experimental data and the process of constructing an electrical model. We employ Keysight Advanced Design System (ADS) for circuit modeling. Specifically, we deduce the parasitic components of the photodiode (PD) equivalent circuit based on single-port reflection measurements. Subsequently, we leverage this information to derive the transit properties of different photodiodes.

The study encompasses five distinct photodiodes (PD-A, PD-B, PD-C, PD-D, PD-E), each characterized by varying absorber and collector thicknesses, as listed in Table 4.1. Additionally, we fabricate photodiodes on each wafer with different optical apertures (15, 18, 20, 22, and 25 μm) to optimize device geometry for the intended application. Increasing the thickness of the absorber layer notably improves the photodiode's responsivity, albeit at the bandwidth cost. Conversely, adjusting the collector thickness impacts both the transit and capacitive properties of the reverse-biased PD, potentially affecting the effective bandwidth of the receiver system. Striking the right balance among these parameters is critical for optimizing overall PD performance.

While this family of PDs are fabricated with Ground-Signal (GS) pads to facilitate flip chip compatibility with a specific platform, each wafer also includes a Ground-Signal-Ground (GSG) pad device corresponding to all five different optical apertures. This arrangement enables direct comparison and facilitates a detailed study of external parasitic contributions to overall performance. Figure 4.1 depicts a microscopic image of the GSG and GS pad devices.

PD	Absorber thickness	Collector thickness
PD-A	d	x
PD-B	1.6d	0.94x
PD-C	1.6d	0.81x
PD-D	1.6d	0.69x
PD-E	1.6d	0.56x

Table 4.1: Absorber and collector thicknesses of the different modeled PDs.

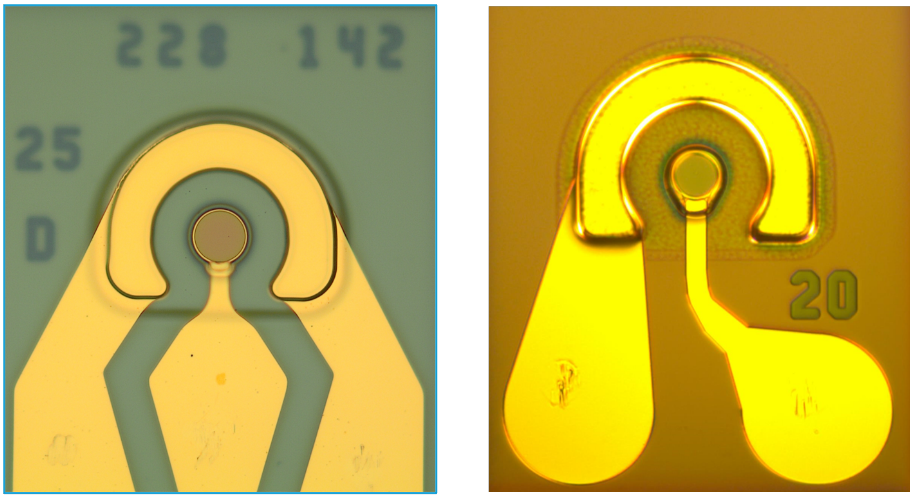

(a) **(b)**

Figure 4.1: (a) PD with GSG and (b) PD with GS pad.

4.1 Parasitic Components

The parasitic component values are determined from the measured single-port reflection data. Subsequently, the circuit depicted in Figure 4.2 is employed to optimize the lumped component values. The vector network analyzer (VNA) measurement yields a complex reflection coefficient (S22) with a 50Ω load. S22 can be correlated to the device impedance Equation (3.7) which in general is a complex quantity with both real and imaginary parts.

4.1.1 Optimization of parasitic components

The component values are determined using the optimization function in ADS. Four distinct optimization goals are defined, each with varying error tolerances. These goals include optimizing the magnitude of S22 (with an error tolerance of up to 2%), the phase of S22 (with an error tolerance of up to 2%), the imaginary part of Z (with an error tolerance of up to 2%), and the real part of Z (with an error

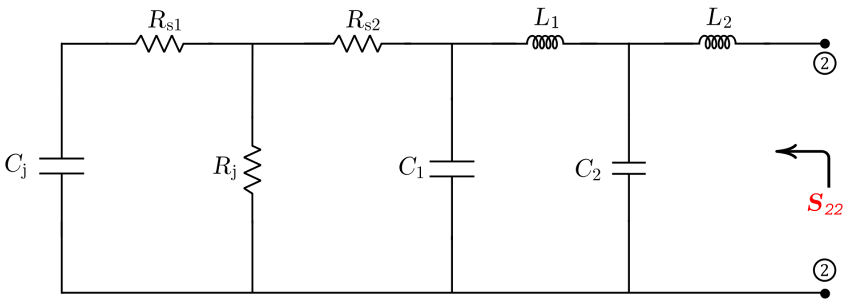

Figure 4.2: Electrical equivalent circuit for single port reflection of PD.

tolerance of up to 6%) for the component extraction process. The optimization process spans a frequency range from 10 GHz to 60 GHz, aligning with the device's area of interest. Initially, the tuning function in ADS is employed to approximate the main component values based on experimental measurements. Subsequently, a random optimization algorithm with 2500 steps refines the lumped element values. Figure 4.3 illustrates the plots for PD-A with GSG pads (20 μm and -2V reverse bias), featuring component values C_j =43.13fF, C_1 = 6fF, C_2 = 23fF, Rs_1 =8.9Ω, Rs_2 =19.16Ω, L_1 = 7pH, L_2 = 23pH.

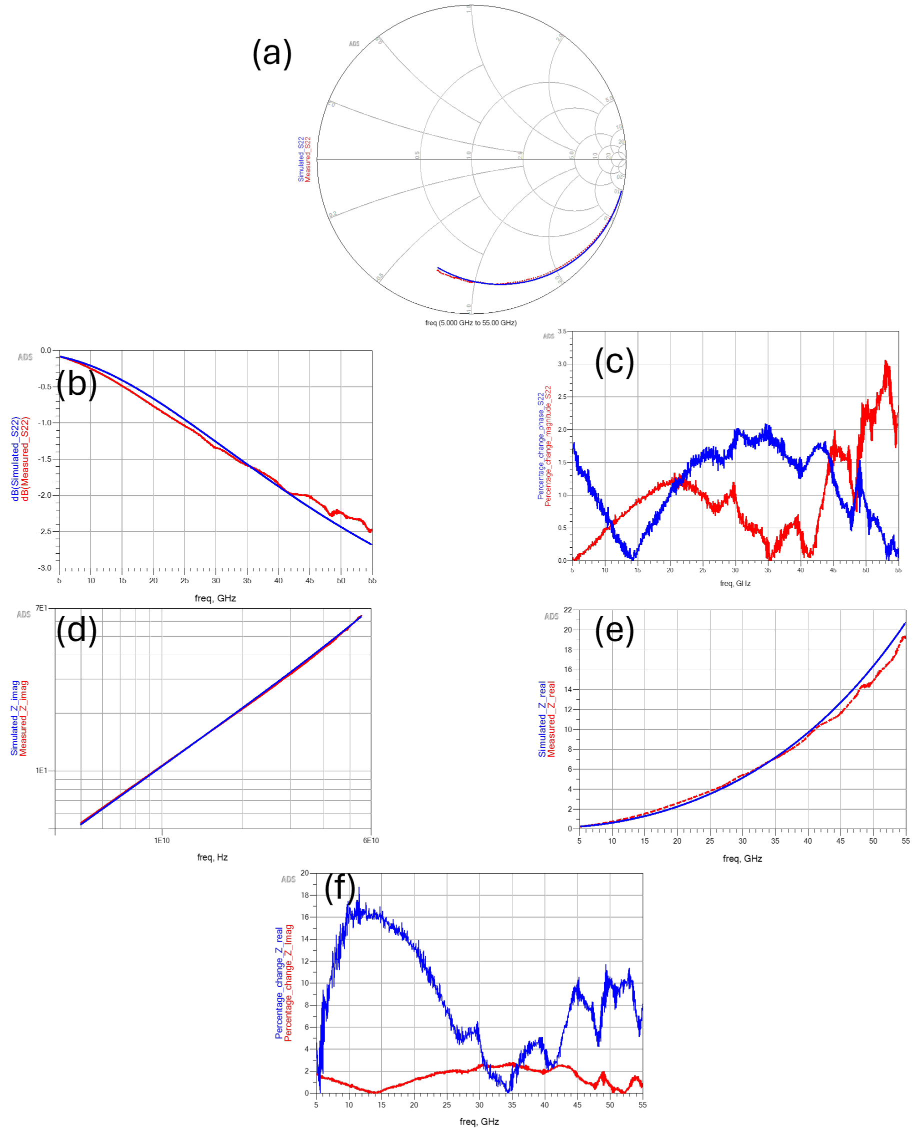

Figure 4.3: Experimental and simulation results of different parameters for 20 μm PD-A with GSG pads at -2V:(a) S22 Smith plot, (b) the magnitude of S22, (c) the percentage error in magnitude and phase of S22, (d) imaginary part of impedance, (e) real part of impedance (f) the percentage error in the real and imaginary part of impedance.

4.1.2 Dielectric bridge and CPW

In the preceding chapter, C1, L1, C2, and L2 correspond to the dielectric bridge and coplanar waveguide components of the device. Regardless of the biasing conditions, these components must remain consistent for each aperture size device. To achieve this, optimization with identical goal definitions is performed across devices of varying aperture sizes and at different bias voltages (-2V, -3V, -4V, -5V). Ideally, one would anticipate that the C1, L1, C2, and L2 values remain constant for a device of a specific aperture size. Consequently, the average values across different bias voltages are used to determine the fixed component values. Figures 4.4, 4.5, 4.6 and 4.7 present the measured and simulated results of PD-A (20 µm), using the C1, L1, C2, and L2 average values, while Table 4.2 provides the corresponding values for the different voltages.

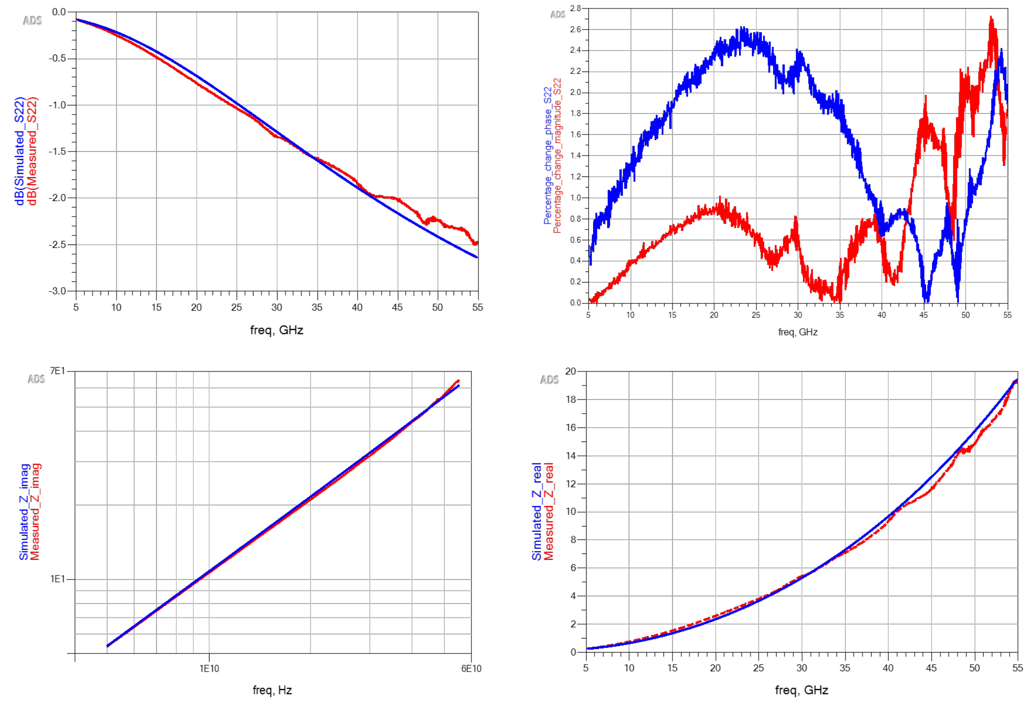

Figure 4.4: Experimental and simulated S22 and impedance results for GSG 20 µm PD-A at -2V bias.

Bias voltage (V)	C1 (fF)	C2(fF)	L1(pH)	L2 (pH)
-2	6	15	3	23
-3	5	16	11	22
-4	6	20	8	24
-5	7	21	6	23
Avg	6	18	7	23

Table 4.2: Lumped element values for different biasing conditions for 20 μm PD-A with GSG pads.

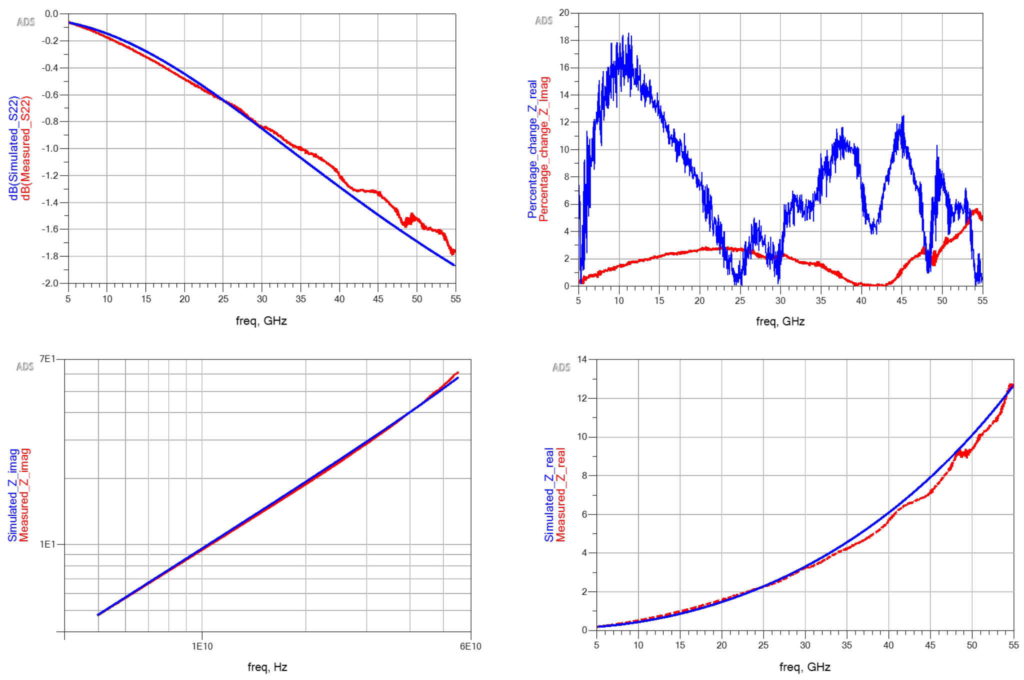

Figure 4.5: Experimental and simulated S22 and impedance results for GSG 20 µm PD-A at -3V bias.

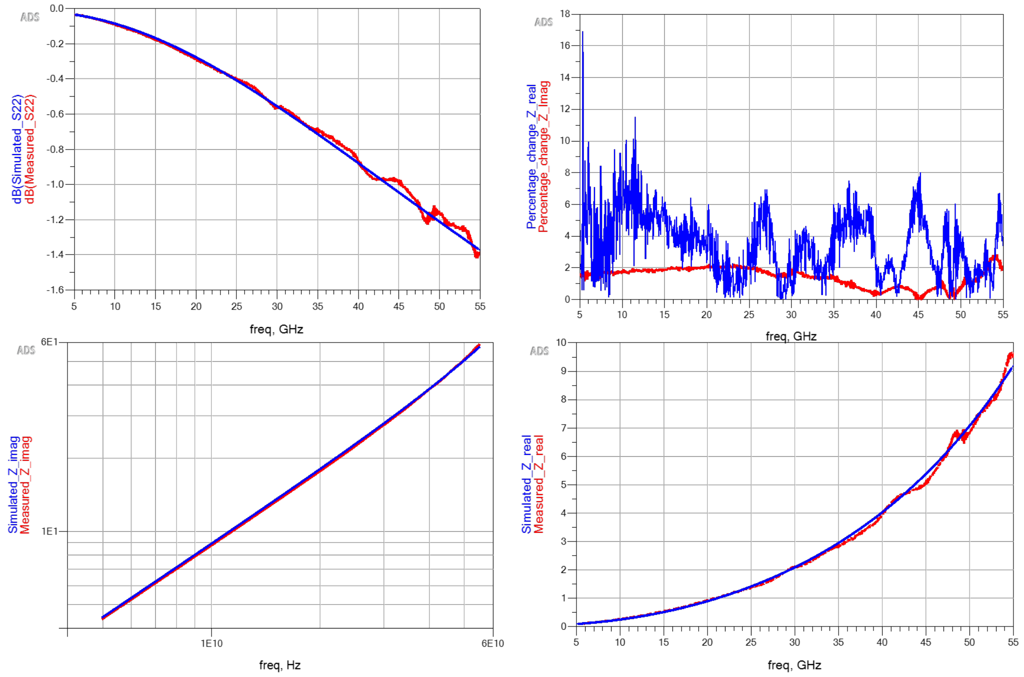

Figure 4.6: Experimental and simulated S22 and impedance results for GSG 20 µm PD-A at -4V bias.

In a similar procedure, lumped element values are extracted for various aperture sizes. The average value across different conditions is then utilized to construct the impedance model for all PDs. PDs with GS pads undergo a similar analysis. Table

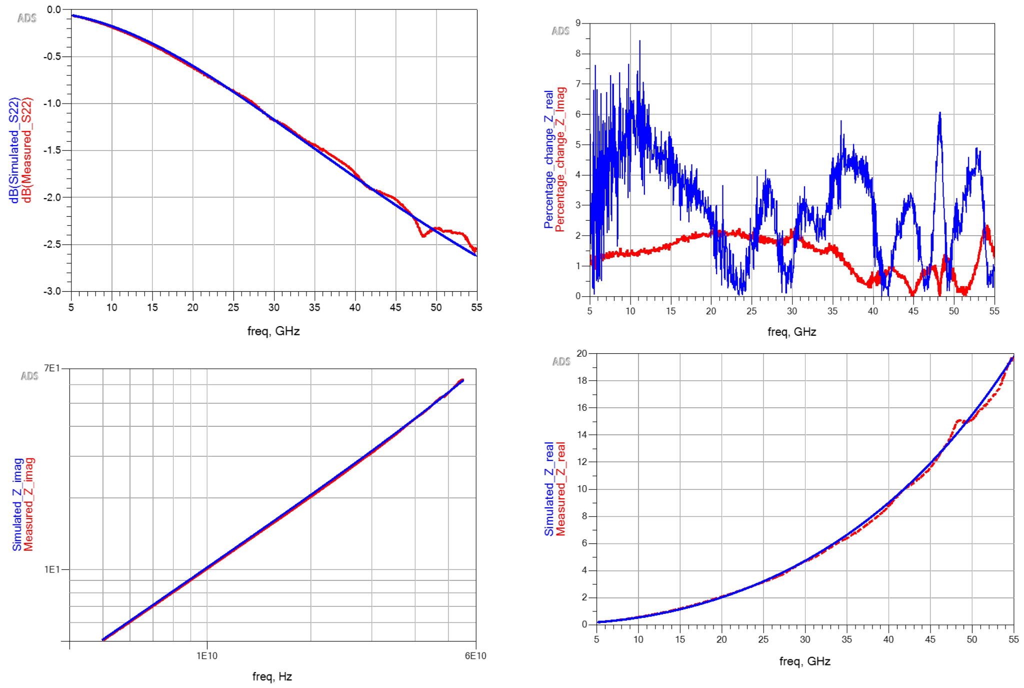

Figure 4.7: Experimental and simulated S22 and impedance results for GSG 20 µm PD-A at -5V bias.

Bias voltage (V)	C1 (fF)	C2(fF)	L1(pH)	L2 (pH)
-2	0.5	15	222	2
-3	1	25	208	5
-4	1.5	20	216	7
-5	1	20	214	6
Avg	1	20	215	5

Table 4.3: Lumped element values for different biasing conditions for 20 μm PD-A with GS pads.

4.3 presents the lumped element values corresponding to various bias conditions, with the average value employed in constructing the equivalent circuit.

4.1.3 Parasitic Response Extraction

After identifying the lumped components for the dielectric bridge and CPW, we analyze the parasitic response of the device using the specified circuit given in Figure 4.8. The circuit's scattering parameters are computed using ADS. In the methodology employed for this study, we focus solely on the S21 magnitude during the modeling process. All other magnitudes are intentionally set to '-100dB', and phase angles are uniformly set to '0'. The bridge and the CPW parameters are established based on a predetermined aperture size, characterized by the mean values of C1, C2, L1, and L2 (given in Tables 4.2 and 4.3). Subsequently, the optimization process is reiterated to ascertain the values of the parasitic elements, specifically (C_j, R_j, R_{s1} and R_{s2}). Table 4.4 provides the values of the parasitic lumped elements for PD-A ($20\mu m$)

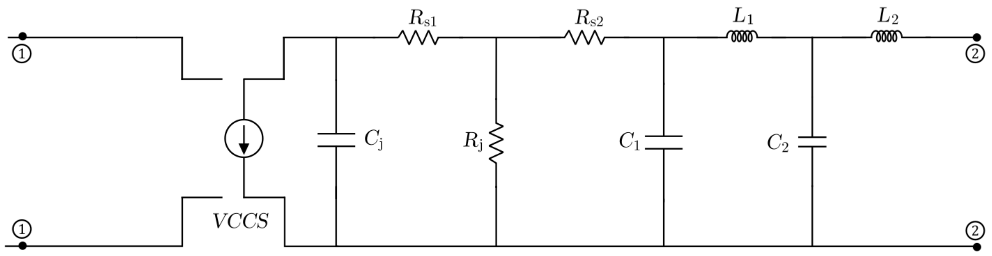

Figure 4.8: electrical equivalent circuit for extracting the parasitic response of the device.

with GSG and GS pad geometry at a biasing voltage of -2V. The device's parasitic frequency response can be accurately simulated by computing the S21 parameter, utilizing the circuit delineated in Figure 4.8. This computation incorporates the lumped element values as specified in Tables 4.2, 4.3 and 4.4. The following plot (Figure 4.9) shows an example of the extracted parasitic response of PD-A (20μm) at -2V bias with GSG and GS pads.

Pad geometry	C_j (fF)	R_j(KΩ)	Rs_1(Ω)	Rs_2 (Ω)
GSG	49	22	9	19
GS	47.8	29	13	11

Table 4.4: Parasitic lumped element values for 20 μm PD-A biased at -2V with GSG and GS pads.

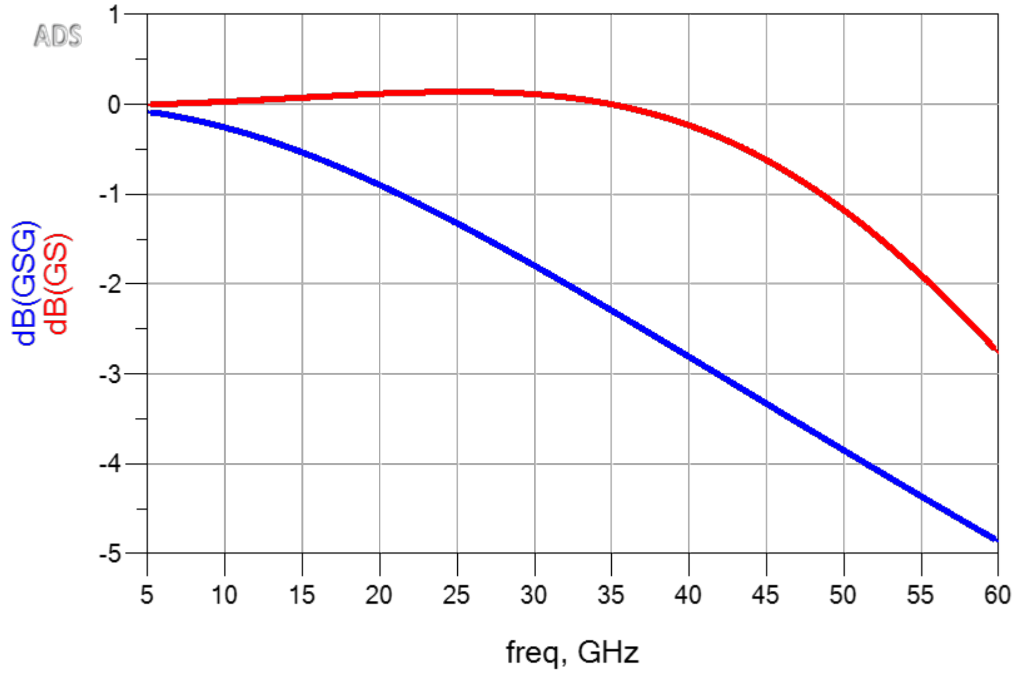

Figure 4.9: Extracted parasitic response of 20μm PD-A biased at -2V with GSG and GS pads.

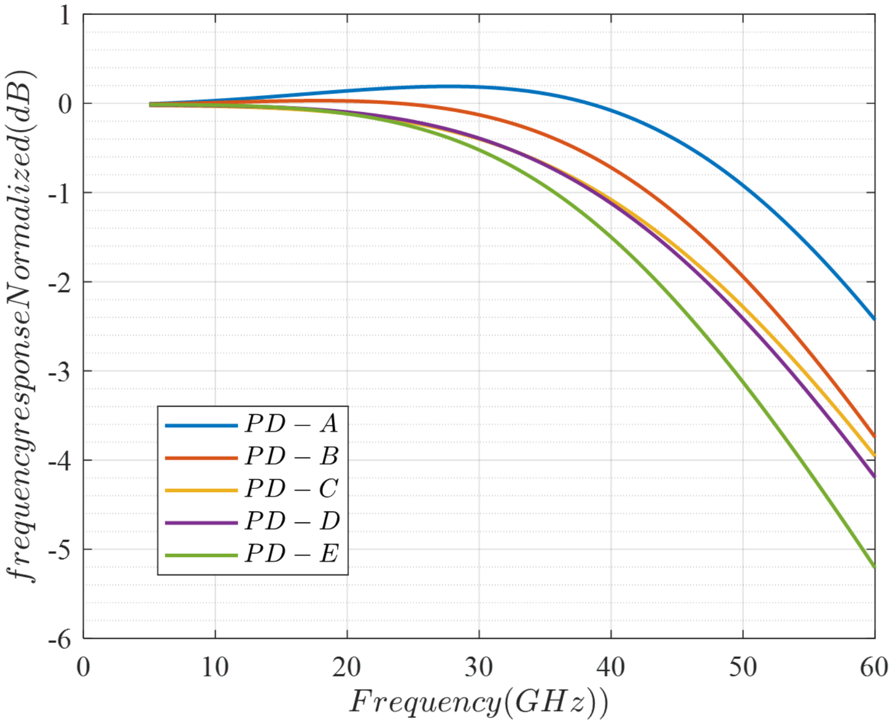

Figure 4.10: Extracted parasitic response of different 20μm PDs biased at -2V.

The effect of high inductance in GS pad devices is well manifested in the peaking parasitic response of the device. It is anticipated that this will have a significant impact on the device's frequency response as well. In the same procedure, the parasitic response for all the other PDs also generated using their specific parasitic elements. Figure 4.10 shows the parasitic response of different PDs of 20 μm with GS pads at a biasing voltage of -2V.

Table 4.5 presents the extracted parasitic component values for various photodiodes (PDs) with GS pad geometry (20μm, -2v biasing). The peaking frequency of the parasitic response is influenced by the junction capacitance, series resistances, and pad lump elements. Among the devices, PD-A exhibits the lowest junction capacitance (as shown in Table 4.5) and consequently, the highest peaking in the parasitic response. Given that all these devices have the same optical aperture, the dielec-

	C_j (fF)	R_j(KΩ)	Rs_1(Ω)	Rs_2 (Ω)
PD-A	47.8	29	13	11
PD-B	54.2	33	17	7
PD-C	51.6	28	14	17
PD-D	54.8	29	18	10
PD-E	64.8	39	13	10

Table 4.5: Parasitic lumped element values for 20μm PDs with GS pad geometry biased at -2V.

tric bridge and CPW lumped elements remain constant. Therefore, the parasitic response of the device is determined solely by C_j,Rs$_1$ and Rs_2.

4.2 Transit Response Extraction

The transit response of a photodiode refers to the time it takes for charge carriers (electrons and holes) generated by incident light to travel across the photodiode's depletion region. The transit response of the device can be deduced from the measured frequency response, utilizing the parasitic lumped elements (extracted parasitic components in the previous section). In this study, Ground-Signal-Ground (GSG) devices are employed to extract the transit response. The parasitic response, illustrated in Figures 4.2 and 4.10, is de-embedded from the measured frequency response (performed in ADS) to isolate the device's transit response. To enhance accuracy and mitigate the impact of device aperture size, we compute the average transit response across various device sizes obtained through the de-embedding process. Figure 4.11 illustrates the transit response of PD-A at a reverse bias of -2V, obtained through the de-embedding process that removes the parasitic response from the device's frequency response. The simulated transit time is derived from the physics-based simulation of the device structure. The simulated transit bandwidth is slightly lower than the extracted values, potentially due to deviations in doping levels from the design. These deviations can result in varying transit speeds

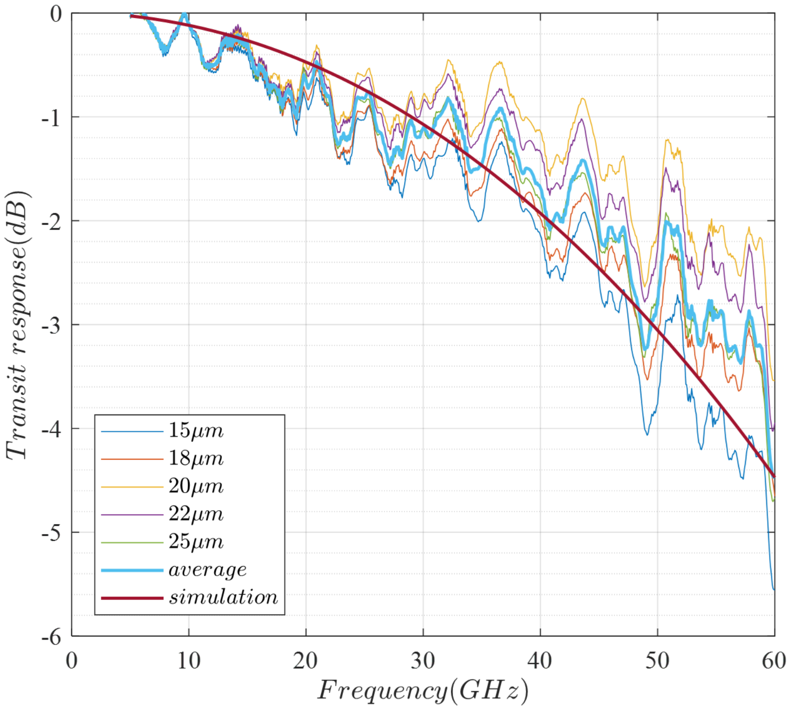

Figure 4.11: Extracted transit responses of of PD-A at -2V bias with the simulation result

or shorter effective transit lengths, which enhance bandwidth at the expense of increased capacitance.

Adhering to the established methodology, the transit response of all photodiodes (PDs) is derived from the measured frequency response using the parasitic response, which is deduced from the parasitic elements calculated for the respective device. Figure 4.12 illustrates the transient response of the PDs featuring a 20 μm aperture, under a bias voltage of -2V. The absorber layer thickness in PD-B, PD-C, PD-D, and PD-E is 1.6 times greater than that of PD-A, which would typically suggest a higher transit bandwidth for PD-A. However, as shown in Table 4.1, the collector layer thickness of the different PDs is also gradually reduced. The transit response is thus a combined effect of both the absorber and collector thicknesses. Notably, PD-E exhibits a broader transit response despite having a thicker absorber layer, likely due to its significantly thinner collector region.

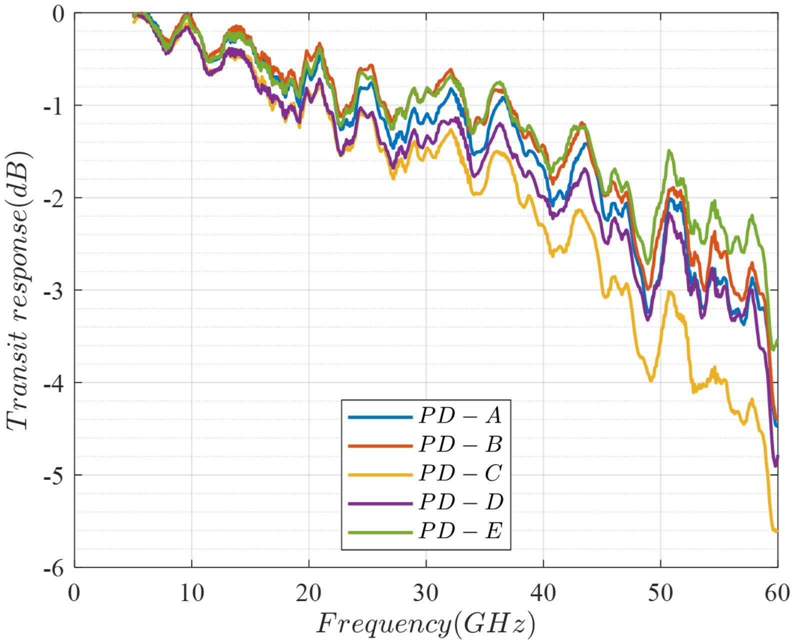

Figure 4.12: Extracted transit responses of 20 μm PDs with GS pads biased at -2V.

4.3 PD Electrical Model

By leveraging the parasitic lumped components derived from optimization based on measured S22 and the extracted transit response of the PD, we construct the electrical equivalent circuit for the PD as shown in Figure 4.13. R_L represents the impedance of the load connected to the PD. We utilize the S parameter associated with the transit to model the transit time for charge carriers within the PD. The S21 value of the circuit, configured with components chosen for the desired bias voltage, yields the simulated frequency response of the device. In the transit S parameter

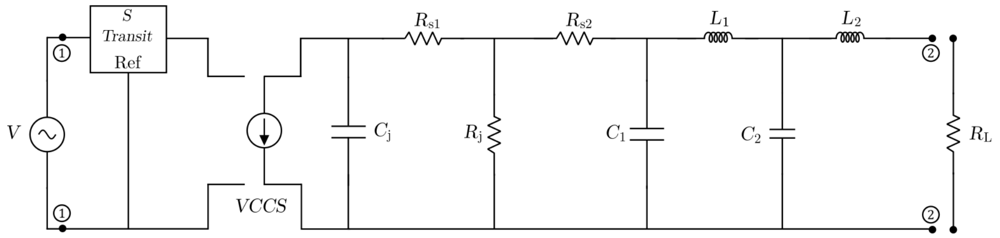

Figure 4.13: PD electrical equivalent circuit.

file, all magnitudes except S21 are intentionally set to '-100dB', and phase angles are uniformly set to '0', aligning with the modeling methodology of interest.
Figure 4.14(a) presents the measured and simulated frequency response of PD-A (GS/20μm) under a reverse bias of -2V. Notably, figure 4.14 (b) highlights the necessity for an additional inductor of 140 pH to align the measured frequency response with the device's simulated behavior. This additional inductance can be attributed to the GS probe, which is not fully accounted for, as only the magnitude of the probe's frequency response is de-embedded for the impulse response measurements.

4.4 PD TIA co-simulation

Co-simulations of the PD and trans-impedance amplifier (TIA) are conducted using the 4-port S parameters of the TIA as a load for the PD's equivalent circuit. The circuit depicted in Figure 4.15 is employed for these co-simulations. L_b in the circuit diagram refers to the inductance of the bond wire from the PD to the TIA MMIC. The TIA S-parameters are provided by the TIA designers. To represent the transit behavior of the device, the extracted transit S-parameter file is used and the optimized parasitic component values of the corresponding devices are used for the simulation. Figure 4.16 shows the combined frequency response of PD-A and TIA at different bias conditions for the GSG device and Figure 4.17 the corresponding results for the GS device. It is evident from Figure 4.16 and 4.17 that the extra inductance in GS pads produces a peaking in the frequency response. The peak-

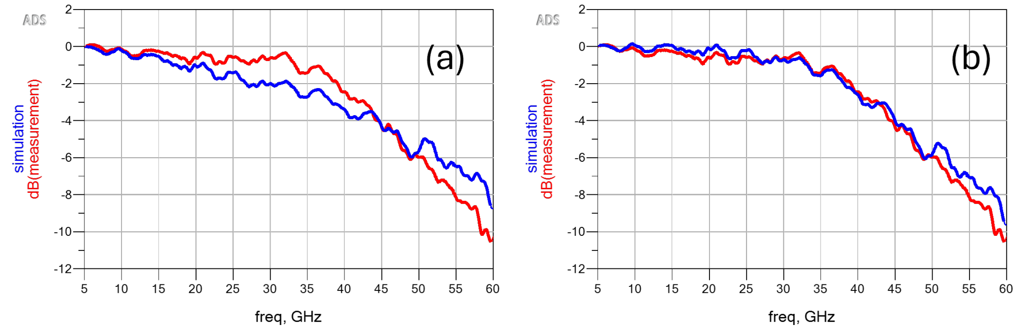

Figure 4.14: Simulated and measured frequency response of 20 μm PD-A biased at -2V. (a) without extra inductor (b) with an extra inductor.

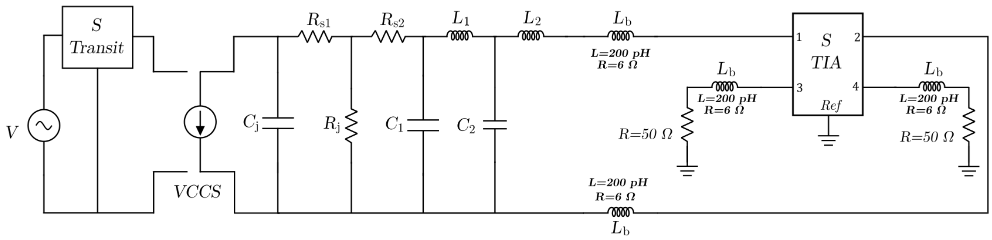

Figure 4.15: Circuit for PD TIA co-simulations.

ing caused by the additional pad inductance results in a flatter frequency response for the GS pad device below 30 GHz. This maintains the system's linearity and prevents frequency-dependent distortions. Additionally, the flat response simplifies system calibration and enables effective utilization of the available bandwidth.

Similarly, the PD (GS pad) and TIA co-simulation is performed for different PDs of aperture size 20 μm at a biasing voltage of -2V. Figure 4.18 presents the normalized frequency response of these PDs in conjunction with the TIA.

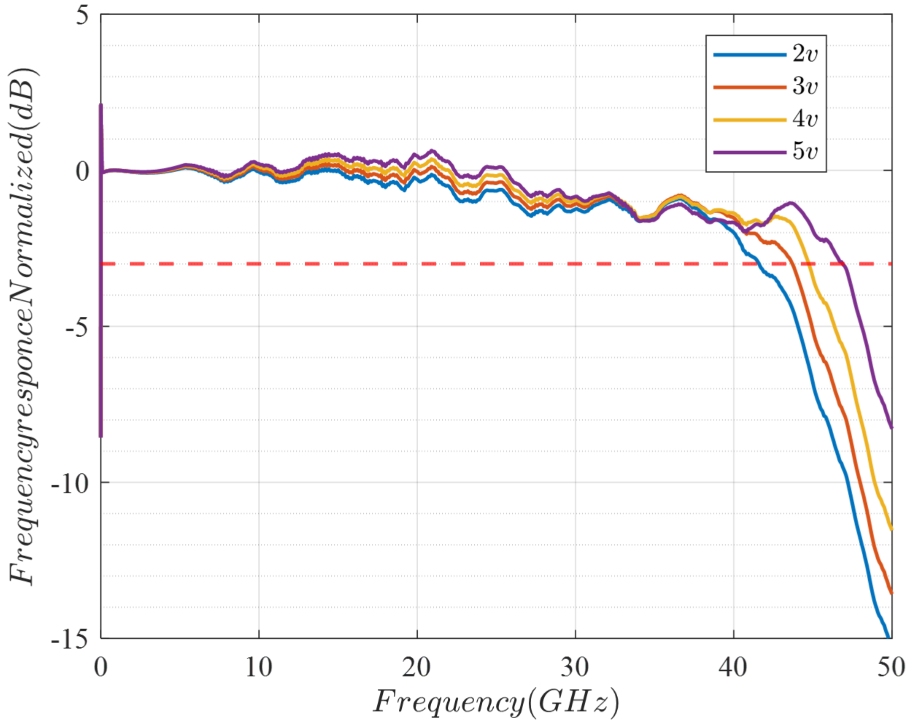

Figure 4.16: Combined frequency response of 20 μm PD-A with GSG pads together with the TIA at different bias voltages.

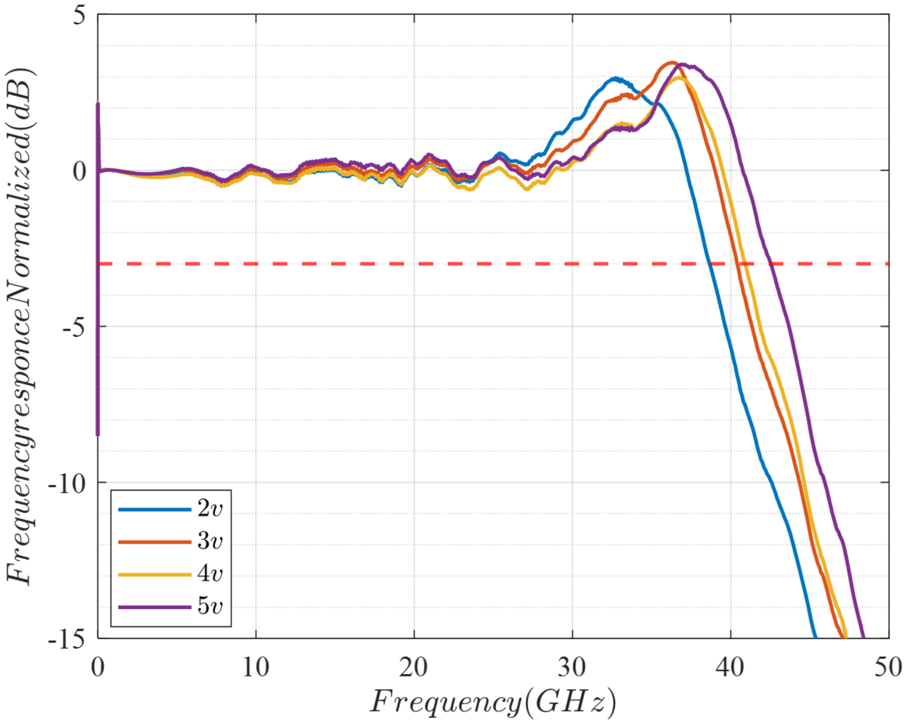

Figure 4.17: Combined frequency response of 20 μm PD-A with GS pads together with the TIA at different bias voltages.

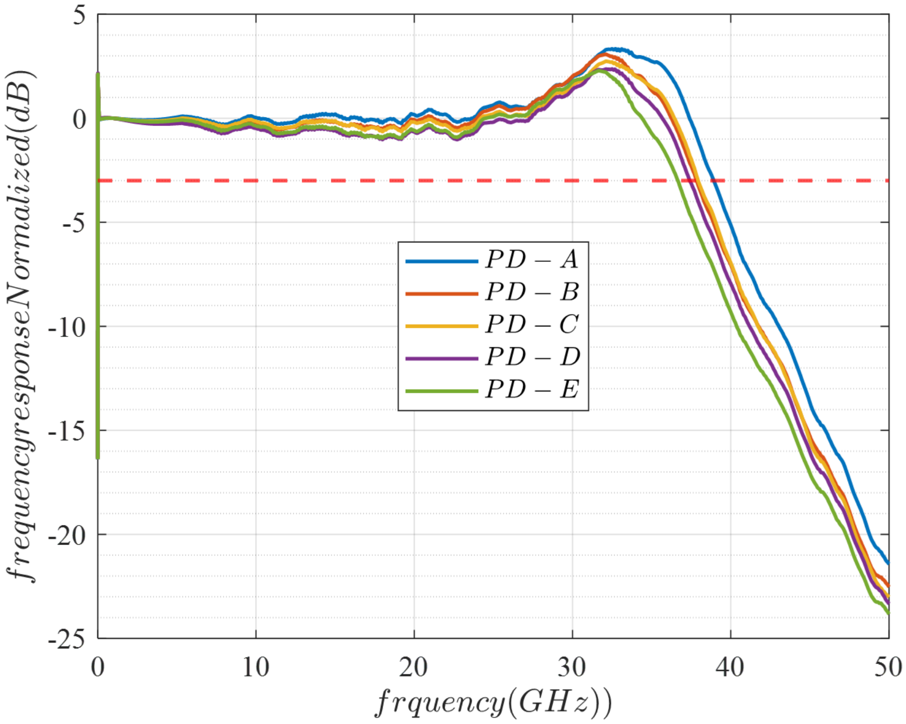

Figure 4.18: Normalized frequency response of different GS 20μm PDs biased at -2V together with TIA.

Among the different designs, PD-A, which has the minimum junction capacitance, exhibits the maximum peaking in the frequency response together with the TIA. Reducing the thickness of the collector layer enhances the device's transit bandwidth but conversely increases its capacitance, resulting in a reduced overall bandwidth. PD-E, with the minimum collector thickness and maximum capacitance, demonstrates the lowest bandwidth among the devices.

4.5 DC measurements of PDs

As a part of characterizing the device the dark current and the responsivity of different PDs are also measured. Table 4.6 shows the measured responsivity and dark current of different PDs with GS pad geometry of 20 μm aperture at -2V biasing condition.

	PD-A	PD-B	PD-C	PD-D	PD-E
Responsivity(A/W)	0.46	0.58	0.55	0.55	0.55
Quantum efficiency	0.54	0.68	0.64	0.64	0.64
Dark current (nA)	≈10	≈ 0.5	≈ 2	≈ 2	≈ 2
Channel Capacity (Gbits/sec)	58	72	71	71	69

Table 4.6: Measured responsivity, quantum efficiency and dark current of different 20μm PDs with GS pad at -2V biasing

The photodiodes PD-B through PD-E exhibit an enhanced responsivity, which aligns with expectations, attributable to the presence of a thicker absorber layer when contrasted with PD-A (Table 4.6). Nanoampere dark currents are anticipated to have a negligible impact on performance, as TIA noise is expected to dominate provided the dark current remains below 1 μA. The channel capacity calculated using the measured bandwidth, responsivity, and dark current is also given in Table 4.6.

5

Discussion and Conclusion

Various photodiodes (PDs) were electrically modeled based on single-port reflection measurements and frequency response data. The electrical model was constructed with particular emphasis on the geometry of the contact pads. It was observed that the specific geometry of the contact pad significantly impacts the performance of the PD when used in conjunction with a trans-impedance amplifier (TIA). To delineate the parasitic components from the S22 measurements, an initial assessment of the bridge and CPW components is conducted across various geometries. It has been observed that devices featuring a ground-signal (GS) pad geometry exhibit a comparatively higher inductance, which, in turn, markedly affects the frequency response of the device. The transit behavior of diverse devices is determined by de-embedding the parasitic response from the device's measured frequency response. The adopted methodology necessitates the extraction of both transit and parasitic responses under varying bias conditions. Pertaining to the comprehensive electrical model of the PDs with GS pads, an additional inductance of approximately 140 nH is required to replicate the measured frequency response. This supplementary inductance is attributable to the inductance of the GS probe, which is employed for biasing and for the collection of photocurrent from the PD, a characteristic particularly pronounced in GS pad devices.

Notably, the behavior of ground-signal pads, as compared to ground-signal-ground pads, indirectly contributes to an inductive peaking effect [29], resulting in a 3dB frequency response enhancement of up to 5 GHz. The study also reveals that the transit response of the photodiode (PD) depends not only on the absorber thickness but also on the thickness of the collector layer. Therefore, it is possible to achieve higher responsivity without compromising the device's transit speed by adjusting the collector layer thickness. However, this adjustment increases capacitance, making it essential to consider the real-world load of the PD to achieve an appropriate trade-off between transit time and capacitance. Among the various designs, PD-A, with the minimum junction capacitance, exhibits the largest bandwidth but also the strongest peak in the frequency response when paired with the TIA. Reducing the collector layer thickness enhances the device's transit bandwidth but conversely increases its capacitance, resulting in a reduced overall bandwidth with the TIA. PD-E, with the minimum collector thickness and maximum capacitance, demonstrates the lowest bandwidth among the devices.

The methodology employed in this study utilizes S22 and frequency response measurements to construct the equivalent circuit. Consequently, the mathematical equations used are sometimes under-determined, making it difficult to fully separate certain variables (e.g., C1 and C2, L1 and L2). The accuracy of S22 and frequency measurement data is crucial, as small errors can lead to inaccuracies in the calculated lumped elements. For GS devices, S22 exhibits significant noise at higher frequencies. Therefore, optimization is performed only up to 50 GHz, which makes the model prone to more errors in high-frequency simulations.

The model could be enhanced by employing 3D electromagnetic modeling of the CPW and the dielectric bridge, allowing for the extraction of lumped elements from the 3D EM simulations.

Bibliography

[1] IBTA. IBTA Launches XDR (800G) InfiniBand Specification. `https://www.fibermall.com/news/ibta-launches-xdr-800g-infiniband-spec.htm`, 2023. [Online; accessed 17-June-2024].

[2] Interplex. How the Rise of Generative AI is Impacting Data Centers and Network Infrastructures. `https://interplex.com/trends/how-the-rise-of-generative-ai-is-impacting-data-centers/-and-network-infrastructures/`, 2023. [Online; accessed 21-April-2023].

[3] Andy Cvengros. In Focus: AI's Influence on Data Center Growth. `https://www.areadevelopment.com/data-centers/Q4-2023/AI-influence-on-data-center-growth.shtml`, 2023. [Online; accessed 21-April-2023].

[4] Sizhu Jiang, Jingyi Wang, MV Ramana Murty, Zheng-Wen Feng, Gim-Hong Koh, Sumtro-Joyo Taslim, Aadi Sridhara, Xinle Cai, Nelvin Leong, David W Dolfi, et al. Development and characterization of 100gb/s 940nm vcsels for multimode optical links. In *Vertical-Cavity Surface-Emitting Lasers XXVIII*, volume 12904, pages 35–40. SPIE, 2024.

[5] Mengyue Xu, Yuntao Zhu, Fabio Pittalà, Jin Tang, Mingbo He, Wing Chau Ng, Jingyi Wang, Ziliang Ruan, Xuefeng Tang, Maxim Kuschnerov, et al. Dual-polarization thin-film lithium niobate in-phase quadrature modulators for terabit-per-second transmission. *Optica*, 9(1):61–62, 2022.

[6] Patrick Runge, Felix Ganzer, Jonas Gläsel, Sebastian Wünsch, Sven Mutschall, and Martin Schell. broadband 145ghz photodetector module targeting 200gbaud applications. In *Optical Fiber Communication Conference*, pages M2A–1. Optica Publishing Group, 2020.

[7] T Ezaki, G Suzuki, K Konno, O Matsushima, Y Mizukane, D Navarro, M Miyake, N Sadachika, HJ Mattausch, and M Miura-Mattausch. Physics-based photodiode model enabling consistent opto-electronic circuit simulation. In *2006 International Electron Devices Meeting*, pages 1–4. IEEE, 2006.

[8] Sheikh Z Ahmed, Samiran Ganguly, Yuan Yuan, Jiyuan Zheng, Yaohua Tan, Joe C Campbell, and Avik W Ghosh. A physics based multiscale compact model of pin avalanche photodiodes. *Journal of Lightwave Technology*, 39(11):3591–3598, 2021.

[9] Jin Li, Bing Xiong, Changzheng Sun, Di Miao, and Yi Luo. Analysis of

frequency response of high power mutc photodiodes based on photocurrent-dependent equivalent circuit model. *Optics express*, 23(17):21615–21623, 2015.

[10] Stephen B Alexander. *Optical communication receiver design*, volume 37. SPIE Press, 1997.

[11] Heinz Beneking. *High speed semiconductor devices: circuit aspects and fundamental behaviour.* Springer Science & Business Media, 1994.

[12] Giovanni Ghione et al. *Semiconductor devices for high-speed optoelectronics*, volume 116. Cambridge University Press Cambridge, 2009.

[13] Gerd Keiser and Gerd Keiser. *Fiber optic communication networks.* Springer, 2021.

[14] John Bowers and Charlesa Burrus. Ultrawide-band long-wavelength pin photodetectors. *Journal of Lightwave Technology*, 5(10):1339–1350, 1987.

[15] Tadao Ishibashi and Hiroshi Ito. Uni-traveling carrier photodiodes: Development and prospects. *IEEE Journal of Selected Topics in Quantum Electronics*, 28(2: Optical Detectors):1–6, 2021.

[16] Qingtao Chen, Xiupu Zhang, Mohammad S Sharawi, and Raman Kashyap. Advances in high–speed, high–power photodiodes: From fundamentals to applications. *Applied Sciences*, 14(8):3410, 2024.

[17] Tadao Ishibashi and Hiroshi Ito. Uni-traveling-carrier photodiodes. *Journal of Applied Physics*, 127(3), 2020.

[18] Anders Gosta Larsson, Attila Fülöp, Oren Steinberg, and Elad Mentovich. High-speed, large-area separate absorption and drift photodetector, September 8 2022. US Patent App. 17/652,989.

[19] Anders Larsson. *Semiconductor Optoelectronics: Device Physics and Technologies.* Department of Microtechnology and Nanoscience, Chalmers University of Technology, 2015.

[20] Herbert Venghaus and Norbert Grote. *Fibre optic communication: key devices*, volume 161. Springer, 2017.

[21] Bowen Song, Bei Shi, Simone Tommaso Šuran-Brunelli, Si Zhu, and Jonathan Klamkin. Low dark current and high speed ingaas photodiode on cmos-compatible silicon by heteroepitaxy. *IEEE Journal of Selected Topics in Quantum Electronics*, 28(2: Optical Detectors):1–8, 2021.

[22] Inder J Bahl. *Lumped elements for RF and microwave circuits.* Artech house, 2022.

[23] G Wang, T Tokumitsu, I Hanawa, K Sato, and M Kobayashi. Analysis of high speed pin photodiode s-parameters by a novel small-signal equivalent circuit model. *IEEE microwave and wireless components letters*, 12(10):378–380, 2002.

[24] Gang Wang, Tsuneo Tokumitsu, Ikuo Hanawa, Yoshihiro Yoneda, Keiji Sato, and Masahiro Kobayashi. A time-delay equivalent-circuit model of ultrafast

pin photodiodes. *IEEE Transactions on Microwave Theory and Techniques*, 51(4):1227–1233, 2003.

[25] G Lucovsky, RF Schwarz, and RB Emmons. Transit-time considerations in p—i—n diodes. *Journal of applied physics*, 35(3):622–628, 1964.

[26] AD Gifford, DA Humphreys, and Paul D Hale. Comparison of photodiode frequency response measurements to 40 ghz between npl and nist. *Electronics Letters*, 31(5):397–398, 1995.

[27] R Thomas Hawkins, Michael D Jones, Steven H Pepper, and Jeffrey H Goll. Comparison of fast photodetector response measurements by optical heterodyne and pulse response techniques. *Journal of lightwave technology*, 9(10):1289–1294, 1991.

[28] Tracy S Clement, Paul D Hale, Kevin C Coakley, and Chih-Ming Wang. Time-domain measurement of the frequency response of high-speed photoreceivers to 50 ghz. *NIST SPECIAL PUBLICATION SP*, pages 121–124, 2000.

[29] James J Morikuni and S-M Kang. An analysis of inductive peaking in photoreceiver design. *Journal of lightwave technology*, 10(10):1426–1437, 1992.

DEPARTMENT OF MICROTECHNOLOGY AND NANOSCIENCE
CHALMERS UNIVERSITY OF TECHNOLOGY
Gothenburg, Sweden
www.chalmers.se

CHALMERS
UNIVERSITY OF TECHNOLOGY